

The effect of large U_d on the Raman spectrum in the copper-oxide superconductors

H. Nikšić^a, E. Tutiš^b and S. Barišić^a

^aDepartment of Physics, Faculty of Science, Bijenička 32, POB 162, Zagreb, Croatia

^bInstitute of Physics, Bijenička 46, POB 304, Zagreb, Croatia

ABSTRACT

The effect of the charge fluctuations on the electronic and Raman spectrum of high temperature superconductors is examined, using the slave boson approach to the large Coulomb repulsion U_d on the copper site. Instead of the saddle point approximation $\langle b \rangle \neq 0$ for the slave boson, characteristic for various $N \rightarrow \infty$ approaches, we confine ourselves to the non-crossing approximation (NCA) diagrams for the Green functions. In this way the effects of charge fluctuations and of the constraint of no double occupancy on the copper site on the shape of the electronic spectrum are studied primarily, while the slave boson diagrams responsible for copper-copper spin correlations are intentionally not included. The novel feature of the charge fluctuation dynamics shows up in the slave boson spectrum as the plateau extending over the range of 1eV below $\omega = 0$. This is further reflected in the electronic Raman spectrum that we calculate for various combinations of the polarization of the incoming and scattered light. The Raman spectrum shows the characteristic featureless behaviour up to frequencies of the order of 1eV while the polarization dependence is also in qualitative agreement with experiment.

RUNNING TITLE : The effect of large U_d on the Raman spectrum

KEYWORDS : Raman scattering, electronic structure, normal state properties

1 Introduction

The attention which the copper-oxide superconductors have been attracting in recent years is due to their extraordinarily high transition temperature to the superconducting state. The interest in normal state properties stems from the belief that a better understanding of these properties could give a clue to the superconducting mechanism itself. The Raman spectrum, and especially its continuous, almost featureless, background spreading up to the frequencies of the order of 1eV, is one of the most remarkable of these properties [1, 2]. Considering the energy scales involved it is natural to ascribe this background to the electronic excitations in the system. In this work we propose a microscopic theory of this phenomenon, which is believed to be a common feature of all copper-oxide superconductors.

Several possibilities for the origin of the Raman background were discussed previously in the literature. We comment briefly on some characteristic ones. First, there are theories in which the Raman background is attributed to particular band crossing effects [3]. However, the one-dimensional bands used in the particular case of $\text{YBa}_2\text{Cu}_3\text{O}_{7-y}$ (where they come from the CuO chains) are not expected to be a feature of the copper-oxide superconductors in general. Second, the “Nested Fermi Surface” (NFS) approach [4] starts from the assumption that parts of the Fermi surface have a pronounced nesting property and proceeds by considering the effect of a weak Coulomb interaction. While this approach is certainly an interesting one, various Fermi surface experiments and band calculations indicate that the Fermi surface geometry varies significantly among the HTSC materials, which show the featureless Raman background. Third, the possibility was also considered that the magnetic excitations (paramagnons, related to the antiferromagnetic phase of the pure, undoped compound and common to most HTSC materials) are related to the Raman background, for instance through the coupling of light to the two-magnon excitations.

However, the magnetic exchange constant J , measured by the polarized neutron scattering in pure materials, is not big enough (e.g. $J \approx 1700K$ in $\text{YBa}_2\text{Cu}_3\text{O}_6$, [5] and $J \approx 1400K$ in La_2CuO_4 [6]) to account for the excitations of the order of 8000cm^{-1} . Furthermore, the magnon (paramagnon) excitations presumably become more damped as the doping level is increased and the effective J is significantly suppressed [5], which has been considered and qualitatively understood by several theoretical approaches. On the other hand, it seems that the magnetic excitations indeed contribute to the Raman background around 4000cm^{-1} . This contribution is pronounced [7, 8, 9, 10] in pure and slightly doped materials and fades out on further doping. In fact it seems that this contribution is *superimposed* on an almost uniform, featureless background extending up to $\omega \sim 1\text{eV}$, present in superconductors.

Therefore, in order to understand the origin of this background, we turn towards the role of charge fluctuations and the effect of a strong Coulomb interaction, present in most models of HTSC's. The possibility that the charge fluctuations are responsible for the special properties of the normal phase was suggested by several authors from the very beginning. Varma and collaborators were seeking for the microscopic origin of their marginal Fermi liquid phenomenology in this domain. However, their approach was essentially a weak coupling one while most of the model parameter evaluations give an on-site repulsion U_d on the copper atom which is large relative to the copper-oxygen hybridization, $U_d \gg t_0$. Therefore, we use a strong coupling approach to calculate the effect of large U_d on the Raman spectra. However, the interatomic Coulomb repulsion term V_{pd} , important in their theory, is not included in the present calculation. The effect of the local constraint imposed by the Coulomb repulsion on the Raman spectrum is essential in our approach. In that respect it shares some major physical points with the recent work by Bang [11] in which the t - J model is considered within the more usual approach of the saddle point approximation plus some fluctuation corrections in the slave bosons.

2 Model and method

Following many previous works on the copper-oxide superconductors (refs. [12, 13, 14] and many others) we treat the large Coulomb repulsion U_d in the $U_d \rightarrow \infty$ limit using the slave boson formalism [15, 16, 17]. The application of this formalism is usually accompanied by the immediate use of the saddle point approximation $\langle b \rangle \neq 0$ for the slave boson field b . This approach has successfully accounted for some electronic properties of the system such as the in-gap “band” containing the Fermi level, the large electronic mass and the electronic dispersion of the form found in ARPES experiments. Furthermore, the integration of the high energy (few eV) fluctuations ($\omega \sim \varepsilon_p - \varepsilon_d$) of the boson field around the saddle point adds one more important ingredient to the physics of narrow band fermions - the copper-copper magnetic interaction J_{dd} [18]. However, it is the intermediate frequency range, $\omega < 1\text{eV}$, that must be primarily considered for the explanation of the Raman background. In this region of frequencies, the saddle point approximation does not seem to be an advantageous starting point. In particular, as with any system of noninteracting fermions, the system of effective fermions that emerges on the saddle point level has no intra-band $\vec{k} = 0$ excitations, so that self-energy corrections for fermion lines and vertex corrections in the Raman scattering diagrams are required in order to get a finite Raman response for the frequencies of interest. Furthermore, the spectrum of the Gaussian fluctuations of the slave boson field around their saddle point value shows [19] no sign of the continuum present in the Raman scattering. Also, some fundamental difficulties of the saddle point approach [20] are accompanied by some more practical ones. For example, the \vec{k} -dependence of the boson Green function and the corresponding \vec{k} -space integrals considerably complicate the calculation beyond the saddle point approximation requiring extensive numerical calculations. Actually, the intersite correlation of the bose field should be absent due to the local gauge in-

variance of the model in the slave boson representation, and to the slow fluctuations of the boson phase [21]. Therefore, we do not use the saddle point approximation for the boson field b in our calculations. Instead, we consider the high order diagrams in the boson field, in which the electronic density of states, similar in shape to the one obtained through the saddle point approximation (with the aforementioned in-gap resonance), and the electronic damping, emerge on equal footing [22]. This approach is a direct extension of the treatment of Kroha et al. [23] of the Anderson impurity problem. The model that we use for holes in CuO_2 planes is the well known p - d model [24],

$$H = H_0 + H_{hyb} + H_d , \quad (1)$$

$$H_0 = \sum_{\vec{n}, \sigma} \{ \epsilon_p (c_{x\vec{n}\sigma}^\dagger c_{x\vec{n}\sigma} + c_{y\vec{n}\sigma}^\dagger c_{y\vec{n}\sigma}) + \epsilon_d d_{\vec{n}\sigma}^\dagger d_{\vec{n}\sigma} \} , \quad (2)$$

$$H_{hyb} = \sum_{\vec{n}, \sigma} t_0 [d_{\vec{n}\sigma}^\dagger (c_{x\vec{n}\sigma} + c_{y\vec{n}\sigma} - c_{x\vec{n}-1_x\sigma} - c_{y\vec{n}-1_y\sigma}) + h.c.] , \quad (3)$$

$$H_d = \sum_{\vec{n}} U_d d_{\vec{n}\uparrow}^\dagger d_{\vec{n}\uparrow} d_{\vec{n}\downarrow}^\dagger d_{\vec{n}\downarrow} , \quad (4)$$

in which, apart from the Coulomb repulsion U_d , the parameters ϵ_d , ϵ_p and t_0 denote respectively the energies of the hole in Cu $3d_{x^2-y^2}$ and O $2p(\sigma)$ orbitals and the copper-oxygen hybridization. Transformed to the \vec{k} -space, H_{hyb} , acquires the following form, with the lattice constant set to unity:

$$H_{hyb} = \sum_{\vec{k}, \sigma} \{ d_{\vec{k}\sigma}^\dagger [c_{x\vec{k}\sigma} t_{x\vec{k}} + c_{y\vec{k}\sigma} t_{y\vec{k}}] + [c_{x\vec{k}\sigma}^\dagger t_{x\vec{k}}^* + c_{y\vec{k}\sigma}^\dagger t_{y\vec{k}}^*] d_{\vec{k}\sigma} \} , \quad (5)$$

$$t_{x\vec{k}} \equiv t_0(1 - e^{-ik_x}) , \quad t_{y\vec{k}} \equiv t_0(1 - e^{-ik_y}) . \quad (6)$$

The Hamiltonian simplifies on introducing the bonding and non-bonding combinations of the hole operators on oxygen sites,

$$p_{\vec{k}} \equiv c_{b\vec{k}} \equiv \frac{t_{x\vec{k}} c_{x\vec{k}} + t_{y\vec{k}} c_{y\vec{k}}}{\sqrt{|t_{x\vec{k}}|^2 + |t_{y\vec{k}}|^2}} , \quad c_{n\vec{k}} \equiv \frac{t_{y\vec{k}}^* c_{x\vec{k}} - t_{x\vec{k}}^* c_{y\vec{k}}}{\sqrt{|t_{x\vec{k}}|^2 + |t_{y\vec{k}}|^2}} . \quad (7)$$

Only the bonding combination has an overlap with the copper orbitals. In terms of these operators, the part of the Hamiltonian which describes noninteracting holes

becomes

$$H_0 = \sum_{\vec{k}, \sigma} \left[\epsilon_p \left(p_{\vec{k}, \sigma}^\dagger p_{\vec{k}, \sigma} + c_{n\vec{k}, \sigma}^\dagger c_{n\vec{k}, \sigma} \right) + \epsilon_d d_{\vec{k}, \sigma}^\dagger d_{\vec{k}, \sigma} \right] , \quad (8)$$

$$H_{hyb} = \sum_{\vec{k}, \sigma} t(\vec{k}) [d_{\vec{k}, \sigma}^\dagger p_{\vec{k}, \sigma} + p_{\vec{k}, \sigma}^\dagger d_{\vec{k}, \sigma}] , \quad t(\vec{k}) \equiv \sqrt{|t_{x\vec{k}}|^2 + |t_{y\vec{k}}|^2} . \quad (9)$$

Therefore, from now on we omit the non-bonding states from our discussion [25].

In the slave boson representation [15] in the $U_d \rightarrow \infty$ limit, the fermion operator $f_{\vec{n}\sigma}^\dagger$ is introduced to describe a singly occupied, and the boson operator $b_{\vec{n}}^\dagger$ is introduced to describe an empty orbital state at the copper site \vec{n} . The substitution $d_{\vec{n}\sigma} \rightarrow b_{\vec{n}}^\dagger f_{\vec{n}\sigma}$, which leads to the Hamiltonian in the new representation, is accompanied by a constraint, which separates the physical states from many non-physical ones in the enlarged Hilbert space. In terms of the number operator $Q_{\vec{n}}$,

$$Q_{\vec{n}} \equiv \sum_{\sigma} f_{\vec{n}\sigma}^\dagger f_{\vec{n}\sigma} + b_{\vec{n}}^\dagger b_{\vec{n}} , \quad (10)$$

which commutes with the Hamiltonian, this constraint is written as

$$Q_{\vec{n}} = 1 . \quad (11)$$

In the path integral formulation, the constraint is introduced through the ‘‘Lagrange multiplier’’ $\lambda_{\vec{n}}$ in the partition function [21]

$$Z(Q_{\vec{n}} = 1) = \left\{ \prod_{\vec{n}} \int_{-i\pi/\beta}^{i\pi/\beta} d\lambda_{\vec{n}} \right\} Z(\{\lambda\}) e^{\beta \sum_{\vec{n}} 1 \cdot \lambda_{\vec{n}}} , \quad (12)$$

$$Z(\{\lambda\}) \equiv \int \mathcal{D}b^\dagger \mathcal{D}b \mathcal{D}f^\dagger \mathcal{D}f \mathcal{D}p^\dagger \mathcal{D}p e^{-\int_0^\beta \mathcal{L}(\tau) d\tau} , \quad (13)$$

$$\begin{aligned} \mathcal{L}(\tau) \equiv & \sum_{\vec{n}, \sigma} f_{\vec{n}\sigma}^\dagger \left(\frac{\partial}{\partial \tau} + \epsilon_d \right) f_{\vec{n}\sigma} + \sum_{\vec{n}, \sigma} p_{\vec{n}\sigma}^\dagger \left(\frac{\partial}{\partial \tau} + \epsilon_p \right) p_{\vec{n}\sigma} + \sum_{\vec{n}} b_{\vec{n}}^\dagger \frac{\partial}{\partial \tau} b_{\vec{n}} \\ & + H_{hyb} + \sum_{\vec{n}} \lambda_{\vec{n}} \left(\sum_{\sigma} f_{\vec{n}\sigma}^\dagger f_{\vec{n}\sigma} + b_{\vec{n}}^\dagger b_{\vec{n}} \right) . \end{aligned} \quad (14)$$

The saddle point approximation for the integration over $\lambda_{\vec{n}}$ in (12) fixes $\lambda_{\vec{n}}$ to the value Λ which is, due to the translational symmetry of the system, equal on all copper

sites. Within this approximation, the constraint (11) is satisfied *on the average*,

$$\langle Q_{\vec{n}} \rangle = -\frac{1}{\beta} \frac{\partial}{\partial \lambda_{\vec{n}}} \ln(Z(\{\lambda\})) |_{(\lambda_{\vec{n}}=\Lambda)} = 1 . \quad (15)$$

Following the approach which was previously tested by Kroha et al. [23] on the $U \rightarrow \infty$ Anderson model, with the result that it is in good agreement with those obtained by other methods, we neglect the fluctuations of $\lambda_{\vec{n}}$ around Λ . This means that the states with $Q_{\vec{n}}$ different from unity become allowed. However, the effective Hamiltonian,

$$\begin{aligned} H = \sum_{\vec{k}} \{ & \sum_{\sigma} [\epsilon_p p_{\vec{k}\sigma}^{\dagger} p_{\vec{k}\sigma} + (\epsilon_d + \Lambda) f_{\vec{k}\sigma}^{\dagger} f_{\vec{k}\sigma}] + \Lambda b_{\vec{k}}^{\dagger} b_{\vec{k}} \\ & + \frac{t(\vec{k})}{\sqrt{N}} \sum_{\sigma} [p_{\vec{k}\sigma}^{\dagger} \sum_{\vec{q}} b_{\vec{q}}^{\dagger} f_{\vec{k}+\vec{q}\sigma} + \sum_{\vec{q}} f_{\vec{k}+\vec{q}\sigma}^{\dagger} b_{\vec{q}} p_{\vec{k}\sigma}] \} , \end{aligned} \quad (16)$$

with $\lambda_{\vec{n}}$ fixed to Λ , conserves $Q_{\vec{n}}$, so the states with different $Q_{\vec{n}}$ are not dynamically mixed (N stays for the number of unit cells in the crystal). Therefore, we expect that fixing $\langle Q_{\vec{n}} \rangle = 1$ in our calculation (which itself conserves the Q -charge) will predominantly extract the dynamics of the system with $Q_{\vec{n}} = 1$.

It can be easily checked that, in the absence of the b -condensate, the one-particle Green functions for b and f fields are site-diagonal (or constant in the \vec{k} -space) to all orders in the perturbation $(1/\sqrt{N}) \sum_{\vec{k}, \vec{q}, \sigma} t(\vec{k}) (p_{\vec{k}\sigma}^{\dagger} b_{\vec{q}}^{\dagger} f_{\vec{k}+\vec{q}\sigma} + f_{\vec{k}+\vec{q}\sigma}^{\dagger} b_{\vec{q}} p_{\vec{k}\sigma})$ in (16). In simple words, it is impossible to create (or annihilate) a b or f particle at some site, and then propagate it to some other site, since that would violate the conservation of $Q_{\vec{n}}$.

Further following Kroha et al. [23] we confine ourselves to a non-crossing approximation (NCA) for which the free energy is represented by diagrams given in Fig. 1. Fig. 2 shows the corresponding diagrams for the full Green functions for b , f and p fields. The set of Dyson equations reads as

$$\mathcal{G}_b(\omega)^{-1} = \mathcal{G}_b^0(\omega)^{-1} - \Sigma_b(\omega) , \quad (17)$$

$$\mathcal{G}_f(\omega)^{-1} = \mathcal{G}_f^0(\omega)^{-1} - \Sigma_f(\omega) , \quad (18)$$

$$\mathcal{G}_p(\omega, \vec{k})^{-1} = \mathcal{G}_p^0(\omega)^{-1} - \Sigma_p(\omega, \vec{k}) , \quad (19)$$

with self energies Σ_b , Σ_p and Σ_f of the following form

$$\Sigma_b(\omega) = \frac{1}{N} \sum_{\vec{k}} |t(\vec{k})|^2 \sigma_b(\omega, \vec{k}) , \quad \sigma_b(\omega, \vec{k}) \equiv \frac{2}{\beta} \sum_{\nu} \mathcal{G}_p(\nu, \vec{k}) \mathcal{G}_f(\omega + \nu) , \quad (20)$$

$$\Sigma_p(\omega, \vec{k}) = |t(\vec{k})|^2 \sigma_p(\omega) , \quad \sigma_p(\omega) \equiv \frac{1}{\beta} \sum_{\nu} \mathcal{G}_b(\nu) \mathcal{G}_f(\omega + \nu) , \quad (21)$$

$$\Sigma_f(\omega) = \frac{1}{N} \sum_{\vec{k}} |t(\vec{k})|^2 \sigma_f(\omega, \vec{k}) , \quad \sigma_f(\omega, \vec{k}) \equiv \frac{1}{\beta} \sum_{\nu} \mathcal{G}_b(\nu) \mathcal{G}_p(\omega - \nu, \vec{k}) . \quad (22)$$

The bare Green functions are

$$\mathcal{G}_f^0(\omega) = \frac{1}{i\omega - \Lambda - \epsilon_d + \mu} , \quad \mathcal{G}_b^0(\omega) = \frac{1}{i\omega - \Lambda} , \quad \mathcal{G}_p^0(\omega) = \frac{1}{i\omega - \epsilon_p + \mu} ,$$

where μ denotes the chemical potential for holes. The system of equations (17)-(22) has to be solved self-consistently keeping at the same time $\langle Q_n \rangle = 1$. The number of holes per unit cell is fixed by the doping level of the system, $n_p + n_d = 1 + \delta$.

In solving the system of equations (17)-(22), we transfer them, by means of usual methods of analytic continuation [26] to the expressions in which the integrals over various spectral functions appear. In the numerical integration over frequency a mesh of thousand points per eV is used. Starting with bare Green functions we iterate the complete set of equations until the result does not change any more. Depending on the iteration scheme, the rate of convergence may change considerably, but the same results emerge at the end. For numerical purposes, we use narrow Lorentzians instead of the delta functions for the spectrum of the bare Green functions for fermions. Their widths are typically several times of the mesh size. Once the Green function $\mathcal{G}_p(\omega, \vec{k})$ is known we obtain the Green function for the real hole on the copper site by using the relation

$$\mathcal{G}_d(\omega, \vec{k})^{-1} = \sigma_p(\omega)^{-1} - |t(\vec{k})|^2 \mathcal{G}_p^0(\omega) , \quad (23)$$

shown diagrammatically in Fig.3.

3 Hole spectrum and the local density of states

In this section we present the results for the Green functions, which are obtained on solving the system of equations (17)-(23). For further discussion, we choose parameters [27] $\Delta_{pd} = \epsilon_p - \epsilon_d = 4.0t_0$ (t_0 is of the order of 1eV), $\delta = 0.13$ extra holes per unit cell, and set $\epsilon_p = 0$ for convenience. The values for Λ and μ that correspond [28] to this choice of parameters are $\Lambda = 3.75t_0$ and $\mu = -1.138t_0$. The chemical potential is positioned between the energies ϵ_d and ϵ_p of the copper and oxygen orbitals and the temperature is set to $0.0135t_0$.

For the f -fermion spectrum we get a simple Lorentzian-like peak (Fig. 4), with about 80% of spectral weight in it, positioned on the Fermi level and with the occupancy $n_f = 0.8$ (both spin projections). The structure of the b -boson spectrum is much richer, with a high frequency peak centered at $\omega \sim \Lambda$, and with a tail extending to higher frequencies. For lower frequencies, we find a.) the asymmetric peak at $\omega \approx 0$ and b.) the broad plateau starting from $\omega \approx 0$ and extending beyond -1eV. These features give rise to the following physical hole spectrum.

The hole density of states per spin (hereafter DOS), $-(1/N\pi) \sum_{\vec{k}} \text{Im}G^R(\vec{k}, \omega)$, accumulates (see Fig. 5) around energies ϵ_p (“ p -band”), ϵ_d (“ d -band”) and μ (“ in -gap-band”). While the accumulation near ϵ_p and ϵ_d occurs for physically obvious reasons, the third region may be related to the band that occurs around the renormalized copper energy level in the saddle point approximation [12] for the b field. Experimentally, the “ in -gap” states show directly as a bump in the PES/IPES spectra [29] upon doping. The dispersion that occurs in the “band” around ϵ_p is characterized by the shift of the peaks in $\text{Im}G_p(\vec{k}, \omega)$ towards higher hole energies along the ΓX line in the Brillouin zone. This is in qualitative accordance with a simple tight-binding calculation for the $U_d = 0$ case, except for the fact that now the peaks are of considerable width. The scattering of fermions on the slow boson field resembles the scattering on

the random potential and, similarly to the crystal disorder, increases the relaxation rate for the fermions. The dispersions of the other two “bands” go in the opposite direction (see Fig. 6). Relative intensities of DOS for the oxygen and copper site show that “bands” close to ϵ_p and μ are dominantly of oxygen character, while the “band” around ϵ_d is, as expected, mainly of copper character. The overall result is qualitatively similar to the DOS obtained by carrying out the Gaussian corrections beyond the saddle point approximation in the $1/N$ expansion for the generalized N -component model [30].

At this point the total number of states on the copper and the oxygen atom can be found. The total number of states per spin at the oxygen “site”, given by the integral of $-(1/\pi)\text{Im}G_c^R(\vec{k}, \omega)$, is 1, as it should be. However, the number of states per spin per copper “site” should be 0.5, as one state per copper site is shifted to infinity in the $U_d \rightarrow \infty$ limit, while the integral over $\text{Im}G_d$ gives a somewhat larger number, $0.5 \cdot [1 + (1 - n_f)]$. This deviation can be readily traced back to the $\lambda_{\vec{n}} = \text{const}$ approximation which we use and to the decoupling [31] of b and f fields that takes place in the calculation of σ_p . Indeed, after the analytic continuation to real frequencies, the equation (21) gives

$$\begin{aligned}
-\int \frac{d\omega}{\pi} \text{Im} \sigma_p^R(\omega) &= -\int \frac{d\omega}{2\pi} \{ \text{Im} G_b^R(\omega) \text{cth}(\frac{\omega}{2T}) - \text{Im} G_f^R(\omega) \text{th}(\frac{\omega}{2T}) \} \\
&= \frac{1}{2} n_f + n_b = \frac{1}{2} + \frac{1-n_f}{2} ,
\end{aligned} \tag{24}$$

These extra $(1 - n_f)/2$ states enter into the DOS through the hybridization equations (19) and (23) producing the aforementioned deviation.

One feature of our results which seems alarming when compared with the ARPES measurement of the Fermi surface geometry is that the chemical potential μ , as obtained by the presented selfconsistent calculation, is positioned *above* the peaks in $\text{Im}G(\vec{k}, \omega)$. It means that there is practically no Fermi surface in our calculation, although μ lays inside the in-gap band since the tails in $\text{Im}G(\vec{k}, \omega)$ extend above μ .

The reason for this may be traced back to the position of the peak in $\text{Im } G_b(\omega)$ which is close to $\omega = 0$. The precise position of the peak determines the Fermi surface geometry and the shift of this peak of the order of 0.05eV to lower frequency would cure the problem. We believe that the calculation beyond NCA may produce such a shift restoring the Fermi surface consistent with the experiment. On the other hand, at the energy scales larger than a tenth of an eV the major features of the spectra would presumably remain unchanged in the improved calculation. These energy scales are of the prime interest in further discussion. This concerns in particular the plateau in the boson excitation spectrum which extends over the range [32] of 1eV. In the calculation of the Raman spectra this plateau implies the occurrence of the flat background.

4 Raman spectrum

Before describing the calculation of the Raman spectrum we wish to recall the simple results obtained with the electronic relaxation rate introduced artificially [33]. Using the fermions with the Fermi liquid like relaxation rate $\gamma \approx \omega^2/\Gamma$ gives a Raman spectrum with a *maximum* at the frequency of the order Γ . Further on, such spectra with a maximum are obtained for a wider class of the non-Fermi liquid electronic relaxation rate laws $\gamma \approx \Gamma(\omega/\Gamma)^\alpha$ (with $\alpha > 0$, $\alpha \neq 1$; Γ always being the characteristic energy scale involved) This is in contradiction with the experimentally observed Raman scattering intensity which does not diminish (or which even increases) towards high transfer frequencies of 1eV. The phenomenological marginal Fermi liquid *ansatz* of Varma et al. [34] ($\alpha = 1$ in the above γ) has no such parameter Γ and a linear damping rate for electrons leads to the constant Raman background.

In what follows we do not use any artificial assumption for the electronic spectrum. Instead, we use the boson and the fermion propagators obtained by the numerical

calculation of the preceding section. While it is difficult to draw the correspondence between the aforementioned phenomenological calculation and the ours, it is interesting to note that our plateau in the slave boson spectral function is the feature which leads to the nearly constant Raman background similar to that obtained in the marginal Fermi liquid phenomenology [34].

The calculation of the Raman spectrum proceeds as follows. The coupling of the electromagnetic field to electrons is introduced, as usual, by the substitution

$$t_{r,s}(c_r^\dagger c_s + c_s^\dagger c_r) \rightarrow t(c_r^\dagger c_s e^{\frac{ie}{\hbar c} \int_s^r \vec{A} \cdot d\vec{l}} + c_s^\dagger c_r e^{\frac{ie}{\hbar c} \int_r^s \vec{A} \cdot d\vec{l}}), \quad (25)$$

in the interatomic hybridization term of the original Hamiltonian. This is followed by the expansion of the exponentials up to the terms quadratic in the vector potential \vec{A} . The terms $\vec{p} \cdot \vec{A}$ and $n\vec{A}^2$ describe the coupling of the electromagnetic field to the hole momentum and to the bond charge. As usual, these terms give rise to three different contributions T_a , T_b and T_c to the transition matrix for the Raman scattering. They are shown in Fig. 7 and correspond to

- a) $n\vec{A}^2$ scattering;
- b) $(\vec{p} \cdot \vec{A})^2$ scattering where electron first absorbs the incoming photon with frequency ω_I and then emits the outgoing photon with frequency ω_S ;
- c) similar to b) but with absorption and emission processes taking place in the reverse time order.

The probability for the transition between the initial state $|0\rangle$ (for simplicity we use zero temperature formulae to illustrate further steps) and the final states $|f\rangle$ consistent with the Raman processes described above is equal to

$$W = \frac{2\pi}{\hbar} \sum_f |(T_a + T_b + T_c)_{0f}|^2 \delta(E_0 - E_f). \quad (26)$$

This gives six (three diagonal and three nondiagonal) contributions to the transition probability,

$$W = W_{aa} + W_{bb} + W_{cc} + W_{ab} + W_{ac} + W_{bc} , \quad (27)$$

$$W_{ij} = (2 - \delta_{ij}) \frac{\pi}{\hbar} \sum_f (T_i^* T_j + T_j^* T_i) \delta(E_0 - E_f) , \quad i, j = a, b, c . \quad (28)$$

The Raman spectra that emerge after the numerical integration are shown in Fig. 8. The featureless behaviour that characterizes the resulting Raman spectrum extends approximately up to the frequency of the separation of the “in-gap-band” and the “p-band”. This separation is of the order of 1eV. This agrees with experiment, while scatterings for larger frequencies are not experimentally probed. Above that frequency, our calculations give a sudden increase of the Raman intensity, due to the “interband” processes. Coming back to the spectrum below 1eV, we note that the intensity of the Raman spectrum changes significantly as a function of the polarization of the incident and the scattered light. This is due to the polarization dependence of the electron-light interaction which comes from the nearest-neighbour hopping approximation (see the Appendix for some details). An example of the relative size of contributions which come from various terms in (27) is shown in Fig. 9. The relative importance of various terms changes with polarization (however, the diagonal terms almost always dominate over the nondiagonal ones). In particular, the scattering via the $n\vec{A}^2$ coupling does not contribute at all for the polarization combination (x', y') . In general, the polarization dependence of the intensity of the Raman spectrum shows good qualitative agreement with experimental results. The minor difference in that respect is that the intensity of our spectra for (x, x) and (y', y') polarizations are somewhat lower than the experimental ones [2]. This may point to the necessity of including direct oxygen-oxygen hybridization terms (as well as the corresponding

electron-light coupling terms) in the initial p - d model.

In summary, we have calculated the hole spectrum in the CuO_2 plane, using the slave boson formalism to implement the constraint of no double occupancy on the copper site, and without resorting to the usual saddle point approximation for the slave boson field. A three band density of states structure is obtained, with the Fermi level lying in the “in-gap” band. The corresponding energy scales show up in the Raman spectra, featureless in frequency up to the value of the gap between the “in-gap-band” and the “p-band”. The measured polarization dependence agrees well with our calculation, which is based on the assumption that the Cu-O hopping t_0 is the dominant one in the CuO_2 planes.

This work was supported by the Croatian Government under project 1-03-275 and by the EU-Croatia project CI1*0568-C(EDB).

A Appendix

The polarization dependence (and the corresponding symmetry properties) of the Raman spectrum result directly from the polarization dependence of the electron-light coupling terms in the \vec{k} -space representation. The coupling constants g_1 and g_2 correspond respectively to $\vec{p} \cdot \vec{A}$ and $n\vec{A}^2$ terms. In the p - d model in which only Cu-O hopping is included these coupling constants have the following form:

$$g_{1,\vec{k}}^{dn} \propto -\frac{[(\hat{e}_p \cdot \hat{x})t_{y\vec{k}}\kappa_{x\vec{k}}^* - (\hat{e}_p \cdot \hat{y})t_{x\vec{k}}\kappa_{y\vec{k}}^*]}{\sqrt{|t_{x\vec{k}}|^2 + |t_{y\vec{k}}|^2}}, \quad (29)$$

$$g_{1,\vec{k}}^{dp} \propto -\frac{[(\hat{e}_p \cdot \hat{x})t_{x\vec{k}}\kappa_{x\vec{k}}^* + (\hat{e}_p \cdot \hat{y})t_{y\vec{k}}\kappa_{y\vec{k}}^*]}{\sqrt{|t_{x\vec{k}}|^2 + |t_{y\vec{k}}|^2}}, \quad (30)$$

$$g_{2,\vec{k}}^{dn} \propto -\frac{[(\hat{e}_I \cdot \hat{x})(\hat{e}_S \cdot \hat{x}) - (\hat{e}_I \cdot \hat{y})(\hat{e}_S \cdot \hat{y})]t_{x\vec{k}}t_{y\vec{k}}}{\sqrt{|t_{x\vec{k}}|^2 + |t_{y\vec{k}}|^2}}, \quad (31)$$

$$g_{2,\vec{k}}^{dp} \propto -\frac{[(\hat{e}_I \cdot \hat{x})(\hat{e}_S \cdot \hat{x}) |t_{x\vec{k}}|^2 + (\hat{e}_I \cdot \hat{y})(\hat{e}_I \cdot \hat{y}) |t_{y\vec{k}}|^2]}{\sqrt{|t_{x\vec{k}}|^2 + |t_{y\vec{k}}|^2}}, \quad (32)$$

where

$$\kappa_{x\vec{k}} \equiv it_0(1 + e^{-ik_x}), \quad \kappa_{y\vec{k}} \equiv it_0(1 + e^{-ik_y}) . \quad (33)$$

Here \vec{e}_I and \vec{e}_S denote polarization vectors of the incident and scattered light (in g_1 expressions $\vec{e}_P = \vec{e}_I$ or \vec{e}_S). The superscripts dp and dn stand for the case of the coupling of the light to the copper-bonding and the copper-nonbonding oxygen terms respectively.

References

- [1] T. Staufer, R. Hackl and P. Müller, Solid State Commun. **75** (1990) 975.
- [2] T. Staufer, R. Hackl and P. Müller, Solid State Commun. **79** (1991) 409.
- [3] H. Monien, A. Zawadowski, Phys. Rev. Lett. **63** (1989) 911.
- [4] A. Viroszek, J. Ruvalds, Phys. Rev. Lett. **67** (1991) 1657.
- [5] J. Rossat-Mignod et al., Physica C **185-189** (1991) 86.
- [6] B. Keimer, et al., Phys. Rev. B **46** (1992) 14034.
- [7] D. Reznik, M. V. Klein, W. C. Lee, D. M. Gindberg, S. W. Cheong, Phys. Rev. B **46** (1992) 11725.
- [8] K. F. McCarty, J. E. Schriber, S-W. Cheong, Z. Fisk, Phys. Rev. B **43** (1991) 7883.
- [9] S. L. Cooper, D. Reznik, A. Kotz, M. A. Karlow, R. Liu, M. V. Klein, W. C. Lee, J. Giapintzakis, D. M. Ginsberg, B. W. Veal, A. P. Pauliskas, Phys. Rev. B **47** (1993) 8233.
- [10] S. Tajima, Y. Mizuo, M. Yoshida, T. Wada, Y. Yaegashi, T. Takata, M. Kagiya, N. Koshizuka, H. Yamauchi, K. Tamasaku, S. Uchida, Phys. Rev. B **47** (1993) 12126.
- [11] Y. Bang, Physica C **218** (1993) 251.
- [12] G. Kotliar, P. A. Lee, N. Read, Physica C **153-155** (1988) 538.
- [13] J. H. Kim, K. Levin, A. Auerbach, Phys. Rev. B **39** (1989) 11633.
- [14] D. M. Newns, P. C. Pattniak, M. Rasolt, D. A. Papacontantopoulos, Phys. Rev. B **38** (1988) 7033.

- [15] S. E. Barnes, J.Phys F **6** (1976) 1375.
- [16] P. Coleman, Phys. Rev. B **29** (1984) 3035.
- [17] N. Read and D. M. Newns, J. Phys. C **16** (1983) L1055; **16** (1983) 3273.
- [18] Q. Si, J. P. Lu, K. Levin, Phys. Rev. B **45** (1992) 4930.
- [19] Instead, it reflects the interband and intraband (absent for $\vec{k} = 0$) excitations of the fermions in the renormalized bands. There is also the zero sound mode while the most pronounced feature in the slave boson spectrum is the charge transfer excitation appearing as a peak at the relatively high frequency of the order of the unrenormalized oxygen-copper level separation Δ_{pd} .
- [20] By virtue of the phase fluctuations $\langle b \rangle = 0$ and there is no real condensate [21]. Also, the saddle point approximation is usually justified by some (eg. number of spin projections in the z direction) $N \rightarrow \infty$ generalization of the original model. For $N = 2$ the saddle point approximation gives $\langle b \rangle \sim 1$ and there is simply no room for a genuine classical field.
- [21] P. Coleman, Phys. Rev. B **35** (1987) 5072.
- [22] In this sense our calculation is the simplest slave boson treatment beyond the simple renormalization of the tight binding parameters for fermions.
- [23] J. Kroha, P. J. Hirschfeld, K. A. Muttalib, P. Wolfle, Solid State Commun. **83** (1992) 1003.
- [24] V. J. Emery, Phys. Rev. Lett. **58** (1987) 2794.
- [25] The non-bonding states do enter again when we calculate the Raman spectrum. However, this introduces the interband transitions which are in the frequency range beyond our consideration.

- [26] A. A. Abrikosov, L. P. Gorkov and I. E. Dzyaloshinski in *Methods of Quantum Field Theory in Statistical Physics*, edited by A. Silverman (Dover Publications, Inc., New York, 1975)
- [27] F. Mila, Phys. Rev. B **38** (1988) 11358.
- [28] In practise it is it is easier to choose Λ , and adjust μ to get $\langle Q_n \rangle = 1$ and then calculate the doping level δ to which this choice corresponds.
- [29] T. Watanabe, T. Takahashi, S. Suzuki, S. Sato, H. Katayamayoshida, Phys. Rev. B **44** (1991) 5316.
- [30] C. A. R. Sa de Melo, S. Doniach, Phys. Rev. B **41** (1990) 6633
- [31] Sh. Feng, J. B. Wu, Z. B. Su, L. Yu, Phys. Rev. B **47** (1993) 15192
- [32] In our calculation with previously specified model parameters, this 1eV scale reflects the separation of the in-gap band and the “oxygen” band. In the more usual saddle point approximation for the slave bosons this would correspond to the renormalized oxygen-copper level separation.
- [33] Our generalization with respect to the calculation of the Raman transition rate for the noninteracting fermions consists in introducing the finite relaxation rate in the electronic propagators. Obviously, this does not account for all features that can appear in the Raman spectrum. In particular, additional terms are required in order to include well defined Raman active collective modes (e.g. phonon or a purely electronic excitation) in the spectrum. However the effect of finite electronic relaxation rate accounts in the simplest way (similarly to the multiphonon scattering in the corresponding frequency range) for the smeared part (i.e. for the background) of the Raman spectrum.

- [34] C. M. Varma et al., Phys. Rev. Lett **63** (1989) 1996; C.M. Varma in *Strongly correlated electron systems*, p. 357 eds. G. Baskaran, A. E. Ruckenstein. E. Tossati, Yu Lu, World Scientific, 1989.

Fig. 1: First few diagrams for the free energy within the *NCA*.

Fig. 2: The diagrams for the Dyson equations for b , f and p fields within the *NCA* approximation. f and b are site-diagonal. Bold lines denote the full Green functions.

Fig. 3: The diagram for the Green function for the hole on the copper site.

Fig. 4: The spectra for the (a) f -fermion and (b) b -boson.

Fig. 5: DOS for (a) the oxygen site and (b) the copper site holes.

Fig. 6: In-gap band dispersion (the one containing the Fermi level) along the ΓX line. The spectra for (a) the oxygen site and (b) the copper site are shown.

Fig. 7: Diagrams for the lowest order contributions to the T-matrix for the Raman scattering.

Fig. 8: Transition probability for the Raman scattering for various polarizations of the incident and scattered light as the function of the transfer energy ω .

Fig. 9: The contributions (W_{aa} , W_{bb} , W_{cc} in (a) and W_{ab} , W_{ac} , W_{bc} in (b)), coming from various T-matrix terms, to the total transition probability W are shown for the (x, x) polarization.

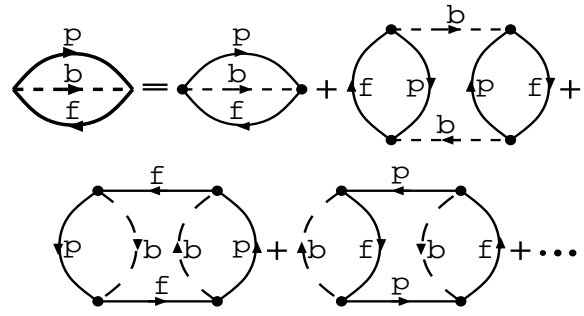


Figure 1:

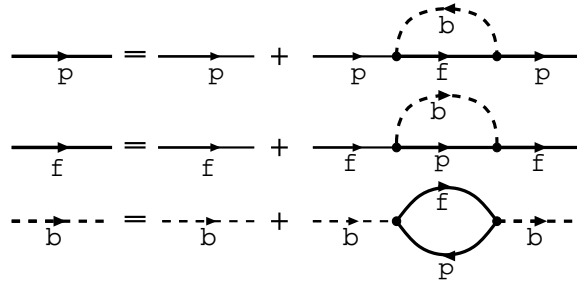


Figure 2:

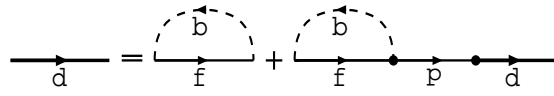


Figure 3:

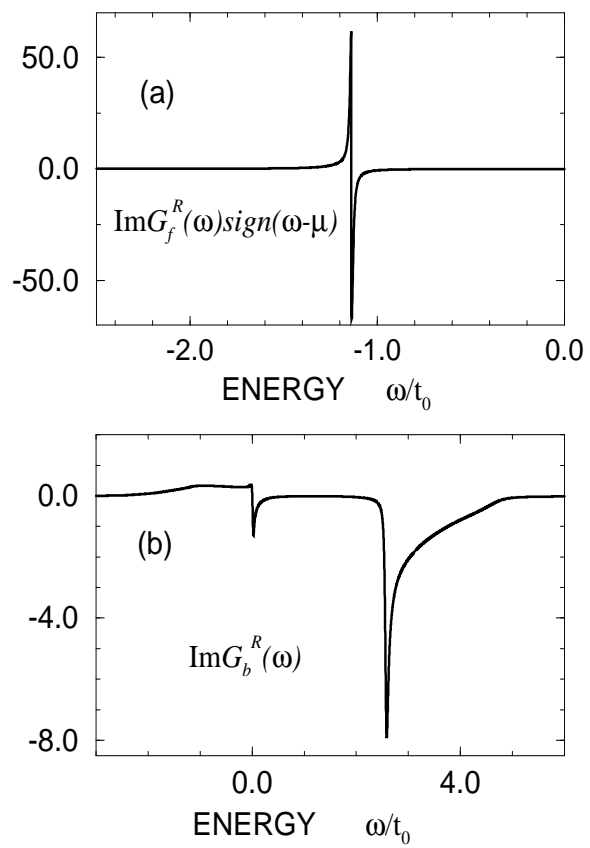


Figure 4:

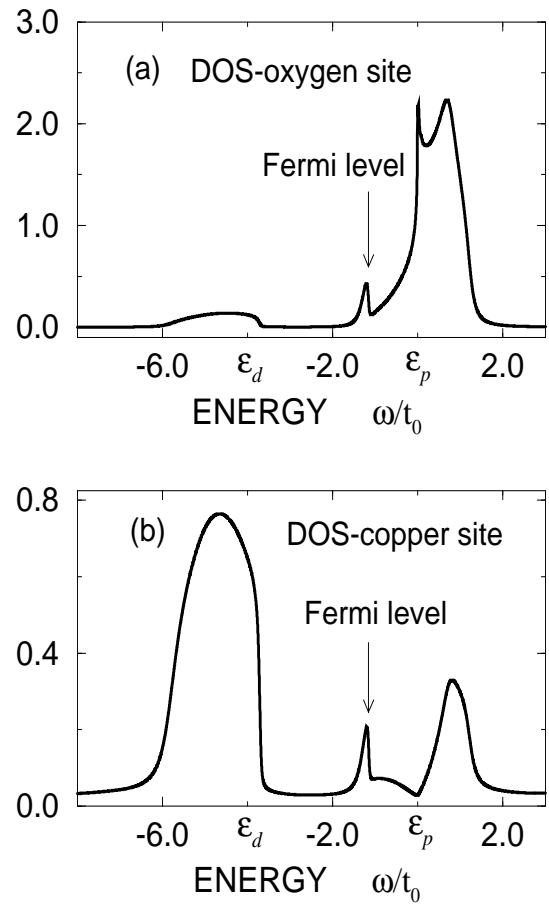


Figure 5:

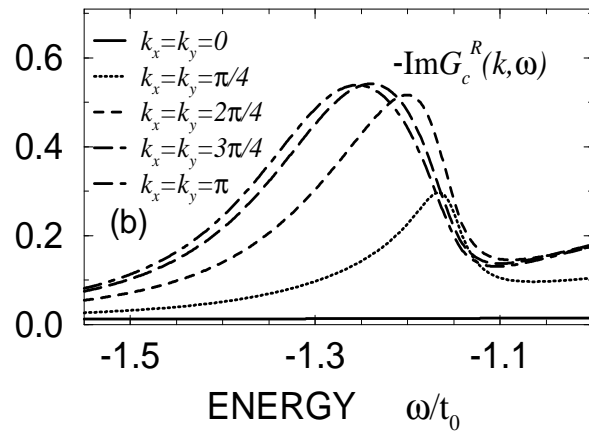
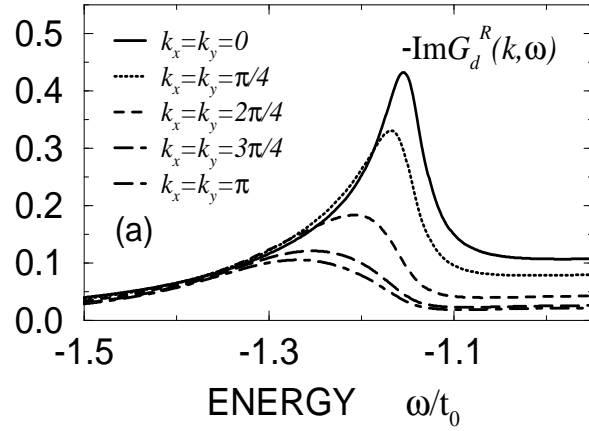


Figure 6:

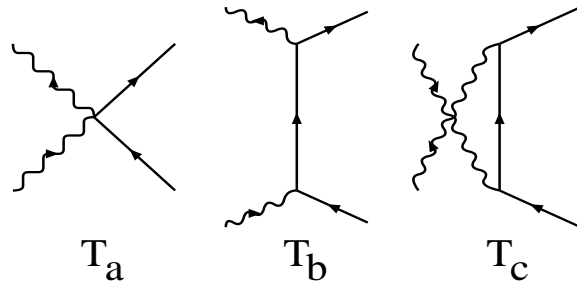


Figure 7:

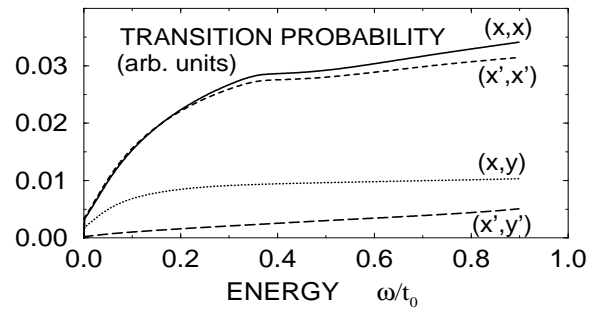


Figure 8:

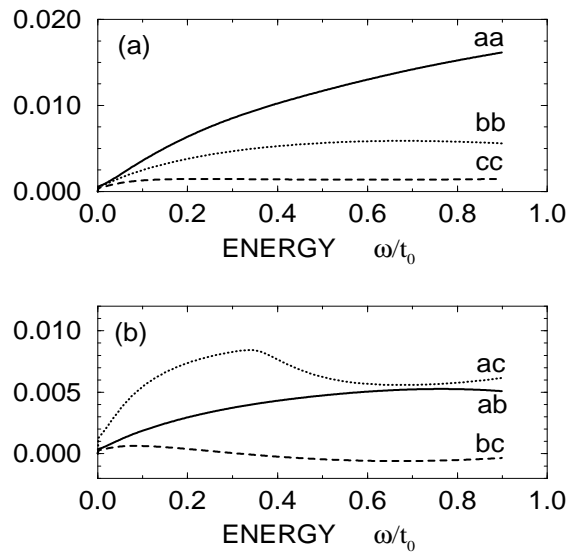


Figure 9: